Applied Physics B (2023) 129:123
https://doi.org/10.1007/s00340-023-08067-y

Applied Physics B
Lasers and Optics

RESEARCH

Unfolding frequency and spatial multimode through parametric amplified cascade four-mode process

Jiajia Wei[1] · Yufeng Li[1] · Binshuo Luo[1] · Jiaxuan Wei[1] · Haitian Tang[1] · Zhou Feng[1] · Changbiao Li[1] · Yanpeng Zhang[1]

Received: 26 April 2023 / Accepted: 26 June 2023 / Published online: 10 July 2023

Abstract

We present a theoretical and experimental investigation of four quantum correlated beams' properties generated through the parametrically amplified cascaded four-wave-mixing (PA-CFWM) process in rubidium vapor. The research explores the signal excitation efficiency of different energy levels by scanning the probe detuning and identifies three different ways to light up the cascade four-mode process. Specially, two pairs of Einstein Podolsky Rosen (EPR) entangled light fields can be generated, leading to a quantum correlation between two previously uncorrelated signals. In addition, the multimode characteristics of output signals are observed in the frequency and spatial domain, and the number of frequency multimode and spatial multimode can be controlled through dressing effect. In our system, the number of spatial modes in four entangled beams can reach up to 1200. Further, the line shift of the PA-CFWM signal resonant frequency can be controlled by experimental parameters, such as the detuning and power of the dressing field. These results are important not only for fundamental tests of quantum effects but also for their numerous applications in quantum technologies, such as quantum imaging and quantum metrology.

1 Introduction

The study of multimode properties has greatly contributed to the development of quantum information technology [1, 2]. Multimode systems expand the capacity of quantum communication systems in the frequency domain and provide more modes with better resolution for quantum entanglement imaging in the spatial domain [3–5]. There are two main types of multimode systems: spatial multimode, which transverses to the direction of propagation (cross-section and divergence), and temporal multimode, which is defined along the direction of propagation (time and frequency). The optical nonlinear effect of the medium is the main mechanism for generating nonclassical multimode light.

Three mainstream methods are used to generate nonclassical multimode light. The first method is the spontaneous parameter down conversion (SPDC) of crystals or quasi-phase-matching crystals based on second-order nonlinear effects [6]. Multimode photons generated by this approach usually has big emission bandwidth. However, its disadvantages of very short coherence time and coherence length limit its application in long-distance quantum communication. The second method is generation of optical parameters including optical parametric amplification (OPA) with no resonant cavity and optical parametric oscillation (OPO) requiring an optical resonant cavity, which is also based on the crystal's second-order nonlinear optical effect [7]. The third method is the non-degenerate four-wave mixing (FWM) process based on third-order optical nonlinear effect without any need for an optical cavity because of the embedded nonlinearity and spatial

Jiajia Wei and Yufeng Li have contributed equally to this work.

✉ Changbiao Li
cbli@mail.xjtu.edu.cn

✉ Yanpeng Zhang
ypzhang@mail.xjtu.edu.cn

Jiajia Wei
1757978758@qq.com

Yufeng Li
1543702761@stu.xjtu.edu.cn

Binshuo Luo
lbsbl8@stu.xjtu.edu.cn

Jiaxuan Wei
597170559@qq.com

Haitian Tang
tht201203@stu.xjtu.edu.cn

Zhou Feng
Second2fz@163.com

[1] Key Laboratory for Physical Electronics and Devices of the Ministry of Education & Shaanxi Key Lab of Information Photonic Technique, Xi'an Jiaotong University, Xi'an 710049, China

separation of the twin output fields [8]. Compared to the first two methods, the FWM system still possesses narrower bandwidth, longer coherence time and coherence length, higher conversion efficiency and spectral brightness [9, 10]. Hence it is expected to be applied in further multimode configurations such as cascaded four-wave mixing (CFWM) process, quantum entangled imaging and long-distance quantum communication.

In the future, quantum technology will be required to generate and control multiple photons and construct a large quantum network. A combination of multiple SPDC processes has been used to obtain entangled multiphoton [4, 11]. Tripartite telecom photons can be generated via a cascaded process [12, 13]. In addition, investigations of the dressing mechanisms and interactions are highly useful for generating high-order nonlinear optical outcomes [14]. And in the hot Rb atomic vapor, the weak probe light of the same frequency is injected into the Stokes signal channel of the spontaneous four-wave mixing process [15], the weak signal will be amplified, and the energy and momentum conservation conditions are satisfied at the same time. A FWM process in hot rubidium vapor is an efficient method to generate and manipulate nonclassical optical nonlinearities, which can successfully generate a pair of multimode intensity-dependent beams and quantum entangled images [16–20]. And the generation of three beams with strong quantum correlation by cascading two four-wave mixing processes in hot atomic vapor has been demonstrated [21]. Even the use of two/multiple pump beams to generate four-mode [22] or ten-mode correlated beams [23, 24] has been demonstrated experimentally or theoretically.

Many investigations have been done on the multimode characteristics. The study of spatio-temporal properties theoretically and experimentally was reported, where a type I LBO crystal is used to generate the spontaneous parametric emission [25]. And a phase sensitive amplification (PSA) achieved via a FWM process in Rb vapor has been researched, which can support at least hundreds of spatial modes [26]. Our group reported the multimode research in a system coexisting of four- and six-wave mixing (SWM) with good responses to the dressing modulation [27] and analysis of multimode spatial and frequency degrees of freedom in a parametric amplified multi-wave mixing (MWM) process where dressing lasers are used to modulate the phase-matching conditions and nonlinear susceptibilities [28]. Nevertheless, the relationship between frequency and spatial multimode as well as spectrum and entanglement imaging based on parametric amplified CFWM entangled four beams is valuable for research.

This paper proposes to generate multimode quantum states by parametric amplified cascaded four-wave mixing process through injection, and study the relationship between frequency multimode and spatial multimode from the analysis of theory and experiment. The frequency domain and the spatial domain correspond to each other through dressing coherent channels, the evolution of a single peak into multiple gain peaks is observed through modulating the detuning, power or angle of the two pump fields. In the spatial domain, the area of the spot becomes larger, and the spatial spot evolves into multiple unevenly distributed light spots.

2 Experimental setup and basic theory

2.1 Experimental setup

Our experiments were performed in a paraffin-coated ^{85}Rb vapor chamber at 125 °C as shown in Fig. 1a, the first strong pump laser beam $\boldsymbol{E}_1$ (frequency ω_1, wave vector $\boldsymbol{k}_1$, and Rabi frequency G_1, vertical polarization) is generated by a tunable semiconductor Topica laser through a tapered laser amplifier, and another pump laser $\boldsymbol{E}_3$ (ω_3, $\boldsymbol{k}_3$ and G_3, vertically polarized) is obtained from the same Toptica laser by beam splitting in a half-wave plate (λ/2) and polarization beam

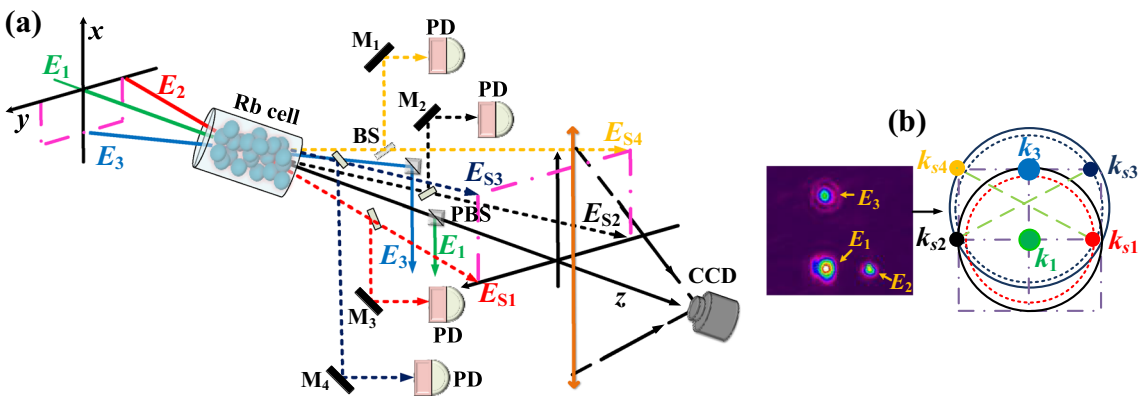

Fig. 1 **a** Simple experimental setup for the PA-CFWM process. **b** Spatial distribution and momentum relations of the light spots

splitter (PBS) and then frequency shifted by an acousto-optic modulators (AOMs) by 0.8 GHz. The angle between the laser beams $\boldsymbol{E}_1$ and $\boldsymbol{E}_3$ generated by the same Toptica laser is 0.48°; the weak probe laser beam $\boldsymbol{E}_2$ (ω_2, $\boldsymbol{k}_2$ and G_2, horizontal polarization) is generated by another Toptica laser, where $G_i=\mu_i E_i/h_i$ ($i=1,2,3$) is the Rabi frequency with transition dipole moment μ_i. When the phase-matching condition in Fig. 1b is satisfied, four FWM processes are generated simultaneously: FWM1 ($2\boldsymbol{k}_1=\boldsymbol{k}_{S1}+\boldsymbol{k}_{S2}$), FWM2 ($\boldsymbol{k}_1+\boldsymbol{k}_3=\boldsymbol{k}_{S1}+\boldsymbol{k}_{S4}$), FWM3 ($\boldsymbol{k}_1+\boldsymbol{k}_3=\boldsymbol{k}_{S2}+\boldsymbol{k}_{S3}$), and FWM4 ($2\boldsymbol{k}_3=\boldsymbol{k}_{S3}+\boldsymbol{k}_{S4}$). And four signal beams $\boldsymbol{E}_{s1}$, $\boldsymbol{E}_{s2}$, $\boldsymbol{E}_{s3}$, and $\boldsymbol{E}_{s4}$ will be formed. To detect the spatial image and spectral intensity of the signal, one branch of the beam splitter is coupled to a charge-coupled device (CCD) for spatial image, and the other to a balanced photodetector (PD) for spectral image.

In Fig. 2a, when the independent laser is used to scan the detuning Δ_{s1} in a large range of the probe field, six different output signals (a–f) appear in the probe ($\boldsymbol{E}_{s1}$) channel. With ω_1—$\omega_{s1}>0$, curves (a–d) in Fig. 2a output signals are obtained, and (e–f) in Fig. 2a output signals are obtained with ω_1—$\omega_{s1}<0$. At the same time, the conjugate ($\boldsymbol{E}_{s2}$) channel, cascade I ($\boldsymbol{E}_{s3}$) channel, and cascade II ($\boldsymbol{E}_{s4}$) channel will appear with b and f output signals. Figure 2b1–b6 shows the energy-level diagrams that correspond to output (a–f) signals. Figure 2b2 shows that the Λ-type atomic energy-level system of the curve (b), which contains two hyperfine ground states $5S_{1/2}[F=2(|1>)$, $5S_{1/2}[F=3(|2>)]$ and a excited state $5P_{1/2}[F=2(|3>)]$. The laser beam $\boldsymbol{E}_1$ acts on the energy levels $|1>\rightarrow|3>$ and $|2>\rightarrow|3>$, and the detuning Δ_1 and Δ_2, respectively. The laser beam $\boldsymbol{E}_2$ transitions at the energy level $|2>\rightarrow|3>$, and the detuning is Δ_{s1}. The laser beam $\boldsymbol{E}_3$ connects the energy levels $|1>\rightarrow|3>$ and $|2>\rightarrow|3>$ with a detuning Δ_3 and Δ_4, respectively. Frequency detuning Δ_i denotes the difference between the resonant transition frequency Ω_i and the frequency ω_i of field $\boldsymbol{E}_i$ ($i=1, 2, 3, 4$). In the large-scale scanning in Fig. 2a, the intensity of the (b) signal is stronger ten times than the (a) signal. The reason is that the detuning of $\boldsymbol{E}_{s2}$ in the (a) signal (Fig. 2b1) is larger by 0.8 GHz than that of the (b) signal (Fig. 2b2), and $\boldsymbol{E}_{s1}$ and $\boldsymbol{E}_{s2}$ signals are generated synchronously, so the (a) signal in probe channel is weak. Similarly, the detuning of the $\boldsymbol{E}_{s2}$ in the (e) signal (Fig. 2b5) is 0.8 GHz larger than that of the (f) signal (Fig. 2b6), so the (e) signal is weak. The low generation efficiency of the (c) and (d) signals in energy level of Fig. 2b3 and (b4) is because of the degenerate energy levels. Meanwhile, the signal gain is also related to the dressing effect. Because the dressing effect is inversely proportional to the detuning of the dressing field, the (e) signal is stronger than (a) signal due to the smaller

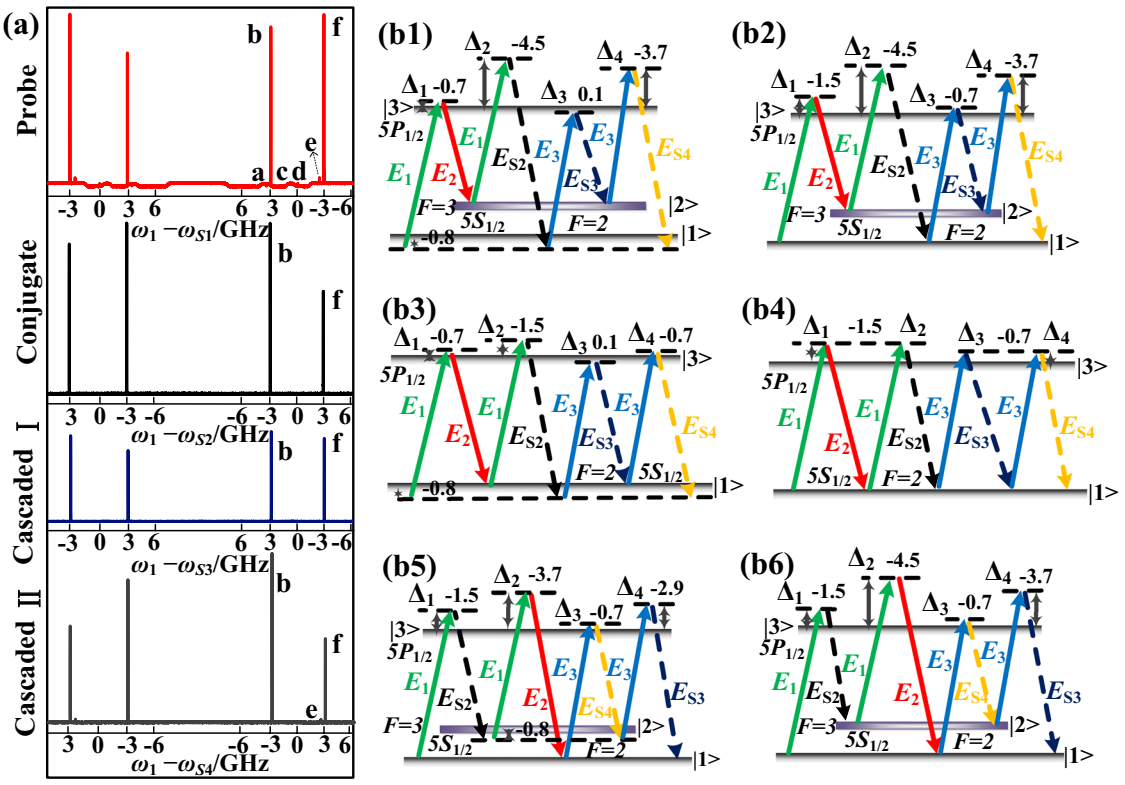

Fig. 2 **a** Measurement of the probe transmission (probe) signal, the corresponding conjugate signal, the cascaded I channel signal, and the cascaded II channel signal varying with the detuning of the probe field. **b1–b6** Energy level diagrams of the a-f peaks

dressing effect by comparing the detuning Δ_1 of the dressing field $\boldsymbol{E}_1$ in Fig. 2b1 and b5.

As shown in Fig. 2b1, when the weak probe $\boldsymbol{E}_2$ is injected into the $\boldsymbol{E}_{s1}$ channel, both FWM1 and FWM2 processes have the injection of probe $\boldsymbol{E}_2$, which is equivalent to two pairs of EPR entangled beams ($\boldsymbol{E}_{s1}$ and $\boldsymbol{E}_{s2}$, $\boldsymbol{E}_{s1}$ and $\boldsymbol{E}_{s4}$) as input signals, corresponding Hamilton quantity are:

$$H_1 = i\hbar(\kappa_1\hat{a}_1^{\dagger}\hat{a}_2^{\dagger}) + \text{H.c.} \tag{1}$$

$$H_1 = i\hbar(\kappa_1\hat{a}_1^{\dagger}\hat{a}_4^{\dagger}) + \text{H.c.} \tag{2}$$

The output signals of two FWM processes are used as input to the PA-CFWM process to generate four brightly entangled beams [30]. Notably, EPR injection affects the quantum properties and produces a PA-CFWM process with high production efficiency [31]. In addition to lighting the PA-CFWM process by two FWM processes as injection, there are also cascaded three-mode processes as injection [32], the first case (CFWM1), $\boldsymbol{E}_{s1}$, $\boldsymbol{E}_{s2}$, $\boldsymbol{E}_{s3}$ signals are injected into the system, equivalent to a pair of strong EPR injections ($\boldsymbol{E}_{s1}$ and $\boldsymbol{E}_{s2}$), and the second case (CFWM2), $\boldsymbol{E}_{s1}$, $\boldsymbol{E}_{s2}$, $\boldsymbol{E}_{s4}$ signals are injected into the system, equivalent to two pairs of strong EPR injections ($\boldsymbol{E}_{s1}$, $\boldsymbol{E}_{s2}$ and $\boldsymbol{E}_{s1}$, $\boldsymbol{E}_{s4}$). The corresponding Hamiltonian for these injections are:

$$H_1 = i\hbar(\kappa_1\hat{a}_1^{\dagger}\hat{a}_2^{\dagger} + \kappa_2\hat{a}_2^{\dagger}\hat{a}_3^{\dagger} + \kappa_3\hat{a}_1^{\dagger}\hat{a}_3^{\dagger}) + \text{H.c.} \tag{3}$$

$$H_1 = i\hbar(\kappa_1\hat{a}_1^{\dagger}\hat{a}_2^{\dagger} + \kappa_2\hat{a}_1^{\dagger}\hat{a}_4^{\dagger} + \kappa_3\hat{a}_2^{\dagger}\hat{a}_4^{\dagger}) + \text{H.c.} \tag{4}$$

and eight-wave mixing processes ($\boldsymbol{E}_{s1}$, $\boldsymbol{E}_{s2}$, $\boldsymbol{E}_{s3}$, and $\boldsymbol{E}_{s4}$) as injection, the corresponding Hamiltonian is:

$$H_1 = i\hbar\kappa_1\hat{a}_1^{\dagger}\hat{a}_2^{\dagger}\hat{a}_3^{\dagger}\hat{a}_4^{\dagger} + \text{H.c.} \tag{5}$$

Theoretically, two generated beams of idle signals $\boldsymbol{E}_{s1}$ and $\boldsymbol{E}_{s3}$ are not in a four-wave mixing process and there is no quantum correlation between them. However, from Fig. 2(a), the cascaded I ($\boldsymbol{E}_{s3}$) channel signal can be observed, indicating that EPR injection causes a quantum correlation between the $\boldsymbol{E}_{s3}$ signal and the $\boldsymbol{E}_{s1}$ signal.

2.2 Frequency multimode

The interaction Hamiltonians of entangled four beams generated by cascaded FWM amplifier can be expressed as

$$H = i\hbar\kappa_1\hat{a}_1^{\dagger}\hat{a}_2^{\dagger} + i\hbar\kappa_2\hat{a}_2^{\dagger}\hat{a}_3^{\dagger} + i\hbar\kappa_3\hat{a}_4^{\dagger}\hat{a}_1^{\dagger} + i\hbar\kappa_4\hat{a}_3^{\dagger}\hat{a}_4^{\dagger} + \text{H.c.} \tag{6}$$

where $\hat{a}_i^{\dagger}$ (i=1,2,3,4) is the boson creation operator that act on the electromagnetic excitation of the anti-Stokes and Stokes channel, $k_1 = -i\varpi_1\chi_1^{(3)}E_1^2/2c$, $k_2 = -i\varpi_2\chi_2^{(3)}E_1E_3/2c$, $k_3 = -i\varpi_3\chi_3^{(3)}E_3^2/2c$, $k_4 = -i\varpi_4\chi_4^{(3)}E_1E_3/2c$, are the pumping parameters of the SP-FWM. The boson creation (-annihilation) operator satisfies the Heisenberg operator equation of motion in the dipole approximation, as follows $\partial E_{s1}/c\partial z = k_1E_{s2}E_1^2 + k_2E_{s4}E_1E_3$, $\partial E_{s2}/c\partial z = k_1E_{s1}E_1^2 + k_2E_{s3}E_1E_3$, $\partial E_{s3}/c\partial z = k_3E_{s2}E_1E_3 + k_4E_{s4}E_3^2$, and $\partial E_{s4}/c\partial z = k_4E_{s3}E_3^2 + k_3E_{s1}E_1E_3$. $\chi_{si}^{(3)} = N\mu_1^2\mu_2^2 * \rho^{(3)}/G^3\hbar^3\varepsilon_0$ can be described by the perturbation chains, where N is atom density, ε_0 is permittivity, and μ_i is the transition dipole moment between the energy levels.

Guided by the Liouville pathway [33], the third-order density matrix elements of $\boldsymbol{E}_{s1}$, $\boldsymbol{E}_{s2}$, $\boldsymbol{E}_{s3}$, and $\boldsymbol{E}_{s4}$ signals can be given by

$$\rho_{S1}^{(3)} = \frac{-iG_1^2G_{S2}}{(\Gamma_{32} + i\Delta_2)(\Gamma_{12} + i\delta_2 + D_1)(\Gamma_{32} + i\delta_2 + i\Delta_1 + D_2)} \tag{7}$$

$$\rho_{S2}^{(3)} = \frac{-iG_1^2G_{S1}}{(\Gamma_{31} + i\Delta_1)(\Gamma_{21} + i\delta_1)(\Gamma_{31} + i\delta_1 + i\Delta_2)} \tag{8}$$

$$\rho_{S3}^{(3)} = \frac{-iG_3^2G_{S4}}{(\Gamma_{32} + i\Delta_4)(\Gamma_{12} + i\delta_4)(\Gamma_{32} + i\delta_4 + i\Delta_3)} \tag{9}$$

$$\rho_{S4}^{(3)} = \frac{-iG_3^2G_{S3}}{(\Gamma_{31} + i\Delta_3)(\Gamma_{21} + i\delta_3)(\Gamma_{31} + i\delta_3 + i\Delta_4)} \tag{10}$$

where Δ_{S1}, Δ_{S2}, Δ_{S3}, and Δ_{S4} represent the frequency detuning of the $\boldsymbol{E}_{S1}$, $\boldsymbol{E}_{S2}$, $\boldsymbol{E}_{S3}$, and $\boldsymbol{E}_{S4}$ signals. Frequency detuning Δ_i denotes the difference between the resonant transition frequency Ω_i and the frequency ω_i of $\boldsymbol{E}_i$. The Δ_1, Δ_2, Δ_3, and Δ_4 are the frequency detuning of the $\boldsymbol{E}_i$ (i = 1, 2, 3, 4) field, respectively. Γ_{ij} = (Γ_i + Γ_j)/2 is the de-coherence rate between |i and |j, $G_i = \mu_{ij}\boldsymbol{E}_i/\hbar$ is the Rabi frequency of $\boldsymbol{E}_i$, δ_i(i = 1,2,3,4) represents the quantum shift of the $\boldsymbol{E}_{Si}$(i = 1,2,3,4) signal, respectively, which can be expressed as $\Delta_{Si} = \Omega_i - \omega_{Si} = \Omega_i - (\varpi_{Si} + \delta_i) = \Delta_i - \delta_i$, then $\delta_i = \Delta_i - \Delta_{Si}$.

Considering the parallel double-dressing effect of $\boldsymbol{E}_1$ and $\boldsymbol{E}_3$, it can be rewritten as: $D_1 = {G_1}^2/(\Gamma_{32} + \mathrm{i}\delta_2 + \mathrm{i}\Delta_1)$ and $D_2 = {G_3}^2/(\Gamma_{12} + \mathrm{i}\delta_2 + \mathrm{i}\Delta_1 - \mathrm{i}\Delta_3)$. When changing the angle α between the pump fields $\boldsymbol{E}_1$ and $\boldsymbol{E}_3$, which is equivalent to adding an additional phase factor $e^{i\Phi}$ to the dressing term, the dressing terms $D_1 = {G_1}^2/(\Gamma_{32} + \mathrm{i}\delta_2 + \mathrm{i}\Delta_1)$ and $D_2 = {G_3}^2/(\Gamma_{12} + \mathrm{i}\delta_2 + \mathrm{i}\Delta_1 - \mathrm{i}\Delta_3)$ can be modified to $D'_1 = {G_1}^2\mathrm{e}^{\mathrm{i}\Phi}/(\Gamma_{32} + \mathrm{i}\delta_2 + \mathrm{i}\Delta_1)$ and $D'_2 = {G_3}^2\mathrm{e}^{\mathrm{i}\Phi}/(\Gamma_{12} + \mathrm{i}\delta_2 + \mathrm{i}\Delta_1 - \mathrm{i}\Delta_3)$.

Also, with $\boldsymbol{E}_2$ and $\boldsymbol{E}_1$ viewed as probe and coupling fields, respectively, the first-order density matrix of the probe transmission signal with dressing effect is EIA (electromagnetic induction absorption), as follows:

$$\rho_{s2}^{(1)} = iG_2/\left[(\Gamma_{32} + i\Delta_{s2}) + |G_1|^2/[\Gamma_{22} + i(\Delta_{s2} - \Delta_1)]\right] \tag{11}$$

With a strong pumping field $\boldsymbol{E}_1$ switched on, the second-order FL signal is generated through the perturbation chain $\rho_{11}^{(0)} \xrightarrow{E_1} \rho_{31}^{(1)} \xrightarrow{-E_1} \rho_{11}^{(2)}$, the diagonal density matrix element is given by:

$$\rho_{FL}^{(2)} = \frac{-|G_1|^2}{(\Gamma_{31} + i\Delta_1 + |G_2|^2/(\Gamma_{21} + i\Delta_1 - i\Delta_2))(\Gamma_{33})} \tag{12}$$

2.3 Spatial multimode

To describe the spatial splitting of the signal $\boldsymbol{E}_{s1}$, $\boldsymbol{E}_{s2}$, $\boldsymbol{E}_{s3}$, and $\boldsymbol{E}_{s4}$ by lasers $\boldsymbol{E}_1$ and $\boldsymbol{E}_3$ beams via kerr nonlinearity, the propagation equations are introduced as following:

$$\frac{\partial E_{s1}}{\partial z} - \frac{i\nabla_\perp^2 E_{s1}}{2k_{s1}} = \frac{ik_{s1}}{n_1}[n_2^{S1}|E_{s1}|^2 + 2n_2^{X1}|E_1|^2 + 2n_2^{X2}E_1E_3]E_{s1} \tag{13}$$

$$\frac{\partial E_{s2}}{\partial z} - \frac{i\nabla_\perp^2 E_{s2}}{2k_{s2}} = \frac{ik_{s2}}{n_1}[n_2^{S2}|E_{s2}|^2 + 2n_2^{X3}|E_1|^2 + 2n_2^{X4}E_1E_3]E_{s2} \tag{14}$$

$$\frac{\partial E_{s3}}{\partial z} - \frac{i\nabla_\perp^2 E_{s3}}{2k_{s3}} = \frac{ik_{s3}}{n_1}[n_2^{S3}|E_{s3}|^2 + 2n_2^{X5}|E_3|^2 + 2n_2^{X6}E_1E_3]E_{s3} \tag{15}$$

$$\frac{\partial E_{s4}}{\partial z} - \frac{i\nabla_\perp^2 E_{s4}}{2k_{s3}} = \frac{ik_{s4}}{n_1}[n_2^{S4}|E_{s4}|^2 + 2n_2^{X7}|E_3|^2 + 2n_2^{X8}E_1E_3]E_{s4} \tag{16}$$

where z is the longitudinal coordinate, k_{si}=$\omega_{si}n_1/c$. n_1 is the linear refractive index,n_2^{S1-4} are the self-Kerr nonlinear coefficients of $\boldsymbol{E}_{s1\text{-}4}$, n_2^{X1-8} are the cross-Kerr nonlinear coefficients of $\boldsymbol{E}_{s1\text{-}4}$ induced by $\boldsymbol{E}_{1,3}$. On the left of the equations above are two terms that describe the beam's longitude propagation and diffraction factor during the propagation of different fields, respectively. On the right side, the first term gives the nonlinear self-Kerr effect, and the rest of the terms describe the nonlinear cross-Kerr effects. Then, the Kerr nonlinear coefficient n_2 values should be evaluated in Rb vapor and can be expressed as:

$$n_2 = \frac{\mathrm{Re}\rho_{si}^{(3)}}{\varepsilon_0 c n_1} = n_2^S + n_2^X = \sum_{i=1}^{4} n_2^{Si} + \sum_{j=1}^{8} n_2^{Xj} \tag{17}$$

The third-order nonlinear self-Kerr density matrix element and cross-Kerr density matrix element are expressed as follows:

$$\rho_{s1}^{s(3)} = \frac{-iG_{s1}|G_{s1}|^2}{\Gamma_{22}(\Gamma_{32} - i\Delta_{s1})^2} \tag{18}$$

$$\rho_{s1}^{x(3)} = \frac{-iG_{S1}|G_3|^2}{(\Gamma_{32} - i\Delta_{S1})(\Gamma_{12} - i\Delta_{S1} - i\Delta_3)(\Gamma_{32} - i\Delta_{S1})} \tag{19}$$

$$\rho_{s1}^{x(3)} = \frac{-iG_{S1}|G_1|^2}{(\Gamma_{32} - i\Delta_{S1})(\Gamma_{12} - i\Delta_{S1} - i\Delta_1)(\Gamma_{32} - i\Delta_{S1})} \tag{20}$$

If the diffraction and self-phase modulation (SPM) terms are ignored, the solutions of Eqs. (13–16) are: $E_{si}(y,z) = E_{si}(y,0)\sum_i \exp(i\varphi_{si}(y))(i = 1,2,3,4)$. The nonlinear phase shift $\varphi_{si}(y)$ can be expressed as $\varphi_{si}(y) = 2k_{s1,s2,s3,s4}n_2I_ie^{-(y-y_i)^2/2}/(n_0I_{s1,s2,s3,s4})$, where I_i is the intensity of the dressing field (coupled field), $I_{s1,s2,s3,s4}$ are the intensity of generated fields, y is the center of $\boldsymbol{E}_1$ in the lateral dimension with $\boldsymbol{E}_{s1}$, $\boldsymbol{E}_{s2}$, $\boldsymbol{E}_{s3}$, and $\boldsymbol{E}_{s4}$ as the origin coordinates. Self-Kerr and cross-Kerr nonlinear effects are critical for achieving large refractive index modulation [29] and are also used to study laser beam self-focusing [27] and image formation [28].

2.4 The spatial multimode due to frequency multimode

The frequency linewidth δ is introduced in calculation of $\chi_{si}^{(3)}$, which causes the wave vector $\boldsymbol{k}$ to change in scale in a spatial degree of freedom as $\Delta k + \delta k = \Delta k + \delta\omega_i n_j/c$, where $\Delta\boldsymbol{k}$ is the phase mismatch and $\delta\boldsymbol{k}$ is the quantum momentum parameter. Therefore, phase mismatching can be quantitatively analyzed by the exact values of frequency resonant linewidth δ_i. It can be seen from this that the frequency mode determines the spatial mode. And n_j represents the reflective index; ω_{si} is defined as the actual frequency of $\boldsymbol{E}_{S1}$ ($_{S2}$, $_{S3}$, $_{S4}$), which is assumed as $\omega_{S1} = \varpi_{S1}$—$\delta_2$—$\delta_3$—$\delta_4$ ($\omega_{S2} = \varpi_{S2} + \delta_2$, $\omega_{S3} = \varpi_{S3} + \delta_3$, $\omega_{S4} = \varpi_{S4} + \delta_4$), and ϖ_{S1} (ϖ_{S2}, ϖ_{S3} and ϖ_{S4}) is the central frequency of ω_{S1}(ω_{S2}, ω_{S3} and ω_{S4}).

Through the third-order nonlinear density matrix element (Eqs. 7–19), we can solve the value of δ_i under different dressing conditions, and the real part of δ_i is the resonance position and the imaginary part is the linewidth. Corresponding results of δ_i are presented in Tables 1, 2, 3. The expressions of the parameters in Tables 1, 2, 3 are $a_{1\pm} = (-\Delta_1 \pm (\Delta_1{}^2 + 4\Gamma_{12}\Gamma_{32} + 4G_1{}^2)^{1/2})/2$; $\Gamma_{e1,e2} = -(\Gamma_{12} + \Gamma_{32})/2 - \Gamma_{12}\Delta_1/2a_{1\pm}$; $a_{2\pm} = (-(2\Delta_1 - \Delta_3) \pm ((2\Delta_1 - \Delta_3)^2 + 4\Gamma_{12}\Gamma_{32} - 4\Delta_1{}^2 + 4\Delta_1\Delta_3 + 4G_3{}^2)^{1/2})/2$; $\Gamma_{e3,e4} = -(\Gamma_{12} + \Gamma_{32})/2 - (\Gamma_{12}\Delta_1 + \Gamma_{32}\Delta_1 - \Gamma_{32}\Delta_3)/2a_{2\pm}$; $a_{3\pm} = (-\Delta_3 \pm (\Delta_3{}^2 + 4\Gamma_{12}\Gamma_{32} + 4G_3{}^2)^{1/2})/2$; $\Gamma_{e5,e6} = -(\Gamma_{12} + \Gamma_{32})/2 - \Gamma_{12}\Delta_3/2a_{3\pm}$; $c_{1\pm} = ((2a_{1+} + \Delta_3) \pm ((2a_{1+} + \Delta_3)^2 - 4(\Delta_3 a_{1+} + \Gamma_{e1}\Gamma_{32} + a_{1+}{}^2)/2$. According to the energy conservation condition of δ_i, ($\delta_1 + \delta_2 + \delta_3 + \delta_4 = 0$), we can define the coherent channels [34]. For instance, from Table 1, coherent channels C_1 and C_2 both satisfy the energy conservation condition: $\delta_1 + \delta_2 + \delta_3 + \delta_4 = 0$. Therefore, 2 coherent channels can be obtained without dressing effect. Similarly, 3 and 4 coherent channels can be obtained from Table 2 for the single-dressing effect and Table 3 for the parallel double-dressing effect, respectively.

Table 1 Coherent channels for PA-CFWM processes without dressing field

Channel	δ_1		δ_2		δ_3		δ_4	
	Resonant position	Line width	Resonant position	Line width	Resonant position	Line width	Resonant position	Line width
C_1	0	$-\Gamma_{12}$	0	Γ_{12}	0	$-\Gamma_{12}$	0	Γ_{12}
C_2	Δ_1	$-\Gamma_{32}$	$-\Delta_1$	Γ_{32}	Δ_3	$-\Gamma_{32}$	$-\Delta_3$	Γ_{32}

Table 2 Coherent channels for PA-CFWM processes with single-dressing field

Channel	δ_1		δ_2		δ_3		δ_4	
	Resonant position	Line width	Resonant position	Line width	Resonant position	Line width	Resonant position	Line width
C_1	Δ_1	$-\Gamma_{32}$	$-\Delta_1$	Γ_{32}	Δ_3	$-\Gamma_{32}$	$-\Delta_3$	Γ_{32}
C_2	$-a_{1+}$	$-\Gamma_{e1}$	a_{1+}	Γ_{e1}	$-a_{1+}$	$-\Gamma_{e1}$	a_{1+}	Γ_{e1}
C_3	$-a_{1-}$	$-\Gamma_{e2}$	a_{1-}	Γ_{e2}	$-a_{1-}$	$-\Gamma_{e2}$	a_{1-}	Γ_{e2}

Table 3 Coherent channels for PA-CFWM processes with parallel double-dressing fields

Channel	δ_1		δ_2		δ_3		δ_4	
	Resonant position	Line width	Resonant position	Line width	Resonant position	Line width	Resonant position	Line width
C_1	$-a_{1+}$	$-\Gamma_{e1}$	a_{1+}	Γ_{e1}	$-a_{1+}$	$-\Gamma_{e1}$	a_{1+}	Γ_{e1}
C_2	$-a_{1-}$	$-\Gamma_{e2}$	a_{1+}	Γ_{e2}	$-a_{1-}$	$-\Gamma_{e2}$	a_{1-}	Γ_{e2}
C_3	$-a_{2+}$	$-\Gamma_{e3}$	a_{2+}	Γ_{e3}	$-a_{3+}$	$-\Gamma_{e5}$	a_{3+}	Γ_{e5}
C_4	$-a_{2-}$	$-\Gamma_{e4}$	a_{2-}	Γ_{e4}	$-a_{3-}$	$-\Gamma_{e6}$	a_{3-}	Γ_{e6}

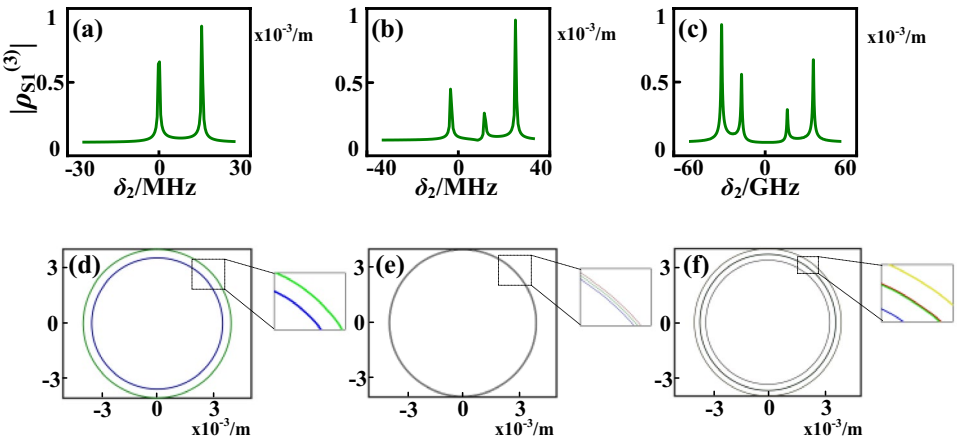

Fig. 3 Third-order nonlinear susceptibility of $\boldsymbol{E}_{s1}$ signals versus frequency linewidth δ_2. **a** Without dressing effect. **b** With $\boldsymbol{E}_1$ field single-dressing effect. **c** With $\boldsymbol{E}_1$ and $\boldsymbol{E}_3$ double-dressing effect. **d–f** Cross-section of output $\boldsymbol{E}_{s1}$ signal cone without dressing, with single and double-dressing effect, respectively

Further, the simulation of nonlinear susceptibility of $\boldsymbol{E}_{s1}$ signal versus δ_2 without dressing laser is shown in Fig. 3a. The results show that $\boldsymbol{E}_{s1}$ signal has two maxima. These two maxima correspond to two CFWM processes existing in the system, and each process satisfies the energy conservation condition. When the dressing field $\boldsymbol{E}_1$ is turned on, we can get three maxima for $\boldsymbol{E}_{s1}$ signal. Furthermore, both the dressing fields $\boldsymbol{E}_1$ and $\boldsymbol{E}_3$ are turned on, and Fig. 3b and c displays four resonant peaks of $\boldsymbol{E}_{s1}$ signal, respectively. The exact roots of δ_2 under different dressing effect are consistent with the resonance positions of δ_2 in Tables 1, 2, 3, respectively. These simulation results suggest more frequency modes in PA-CFWM caused by the dressing effect. Figure 3d–f shows the simulation results of the E_{s1} signal, at a certain cross-section of the pump axis. The number of momentum rings increases with the dressing effect. It indicates that dressing effect will result in more possibility of spatial multimode. The linewidth of δ_i describes the full width at half maximum of the formant in the frequency domain and determines the width of the spatial momentum ring in the spatial domain.

And these results show that the dressing field can control the number of modes in the frequency and spatial domains. Therefore, the δ_i can describe the number of dressing coherent channels and determines how many frequency modes the $\boldsymbol{E}_{Si}$ can generate.

3 Results and discussion

3.1 Frequency multimode analysis

Figure 4a–f, respectively, represents the a, b, c, d, e, and f signal spectrum in the probe channel ($\boldsymbol{E}_{s1}$) at different detuning Δ_1. The detuning Δ_1 corresponding to the a, b, c, and d peaks is − 1.95 GHz, − 1.7 GHz, − 1.55 GHz, − 1.35 GHz, − 1.3 GHz, and − 1.1 GHz in order from top to bottom. The detuning Δ_1 corresponding to the e and f signals is − 1.2 GHz, − 1 GHz, − 0.9 GHz, − 0.8 GHz, − 0.7 GHz, and − 0.55 GHz in order from top to bottom.

Figure 4a and b shows that both the a and b signals contain EIA and third-order gain peak signals ($I_0 - \mathrm{Im}\rho_{S2}^{(1)} + |\rho_{S1}^{(3)}|^2$), which change from the absorption dip near the 85Rb ($F=2$) resonance energy level to near the ^{85}Rb($F=3$) resonance level absorption dip. The EIA signals in the a and b signals first become larger and then become smaller, while the gain peak satisfy the electromagnetically induced transparency (EIT) window ($\Delta_2 - \Delta_{s2} + \Delta_1 = 0$), which increases as it gradually approaches the ^{85}Rb ($F=3$) resonance level absorption dip, with a maximum at $\Delta_1 = -1.1$ GHz. When the frequency shift $\Delta_1 = -1.35$ GHz, the dressing effect of $\boldsymbol{E}_1$ strongly influences the a and b signals. This is because the dressing effect becomes stronger as the generated signal weakens, resulting in the appearance of double and multiple peaks. The ordinate range of Fig. 4a is 0 ~ 0.75, and the ordinate range of Fig. 4b is 0 ~ 2.1. Comparing the optimal gain peak size, we can see that the intensity of b signal is more than three times larger than the a signal.

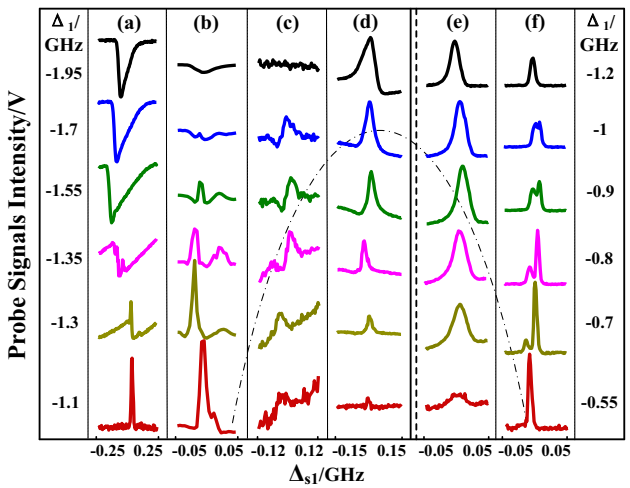

Fig. 4 Measured signal intensities versus laser $\boldsymbol{E}_2$ frequency detuning Δ_{s1} when pumping frequency detuning Δ_1 is set at different discrete detuning. The experimental parameters are: $P_1 = 123$ mW, $P_2 = 127$ μW, $P_3 = 53.5$ mW and $T_{Rb} = 125$ °C. Signal intensities of the a, b, c, and d signals in the probe channel. **a** a signal. **b** b signal. **c** c signal. **d** d signal. **e** e signal. **f** f signal

Figure 4c and d shows that both the c signal and the d signal containing EIA and third-order gain peak signals ($I_0 - \mathrm{Im}\rho_{S1}^{(1)} + |\rho_{S1}^{(3)}|^2$), and the maximum value of the gain peak signal is at $\Delta_1 = -1.35$ GHz and $\Delta_1 = -1.7$ GHz. Different from the change trend of the a and b signals, the third-order gain peak signal ($|\rho_{S1}^{(3)}|^2$) in the c and d signals gradually decreases. It can be explained the c and d signals are absorbed by the ^{85}Rb ($F=2$) resonance absorption dip as the signal gradually approaches the resonance level, and when the value of Δ_1 becomes small, the dressing effect will also enhance and reduce the intensity of the peak. Meanwhile, the first-order signals (linear optical responses) in the a and b signals dominate, while the third-order signals (nonlinear optical responses) in the c and d signals dominateThe ordinate interval of Fig. 4c is 0.18, and the ordinate range of Fig. 4d is 0 ~ 1. Comparing the optimal gain peak size, it is found that the intensity of the d signal is more than twice that of the c signal.

Both the e and f signals contain the third-order gain peak signal ($|\rho_{S1}^{(3)}|^2$) with optimal positions at $\Delta_1 = -0.9$ GHz and $\Delta_1 = -0.55$ GHz, respectively. The ordinate range of Fig. 4e is 0.5 ~ 4.25, and the ordinate range of Fig. 4f is 1.8 ~ 6. Comparing the optimal gain peak, we can see that the intensity f signal is 1.5 times stronger than the e signal. The change from the a signal to the f signal indicates that the signal has changed from a linear optical response dominated to a nonlinear optical response. This is because the signal on the left is close to the ^{85}Rb ($F=3$) and ^{87}Rb ($F=2$) resonance absorption dips, the atomic density and the dipole moment are large, and the dressing effect is strong, so the third-order gain signal is absorbed, and the first-order signal dominates. At the same time, the best gain peak positions from the a signal to the f signal are connected by a curve, and the contour is the shape of a peak. From the results of the analysis of the signals in different energy levels (Fig. 2), it can be seen that the b and f signals have the highest gain, which is consistent with the experimental results in Fig. 4, the energy level with high gain can be selected to produce multimode quantum states.

Figure 5 shows that when the detuning $\Delta_1 = -1.3$ GHz, the b signal of $\boldsymbol{E}_{S1}$, $\boldsymbol{E}_{S2}$, $\boldsymbol{E}_{S3}$, and $\boldsymbol{E}_{S4}$ channels is obtained by scanning the detuning Δ_{s1}. As shown in Fig. 5a2 and a4, the gain peak shows Autler–Townes (A–T) splitting. This is due to the dressing effect of $\boldsymbol{E}_1$ splitting the energy

level $|3>$ into $|G1+>$ and $|G1->$, which can be written as $H|G_{1\pm}\rangle = \lambda_{\pm}|G_{1\pm}\rangle$. The energy-level position is $\lambda_{\pm} = [-\Delta_1 \pm (\Delta_3^2 + 4|G_1|^2)^{1/2}]/2$, and then double peaks from left to right correspond to $|G1+>$ and $|G1->$. The corresponding dressing energy level of $\boldsymbol{E}_{s2}$ and $\boldsymbol{E}_{s4}$ is shown in Fig. 5b2 and b4. However, Fig. 5a1 and a3 shows three peaks, and the dressing effect of $\boldsymbol{E}_3$ should be considered. The energy level |G1-> is divided into two secondary dressing states ($|G3-+>$ and $|G3-->$) due to the dressing effect of $\boldsymbol{E}_3$. Therefore, from left to right, three gain peaks appear. The corresponding dressing energy level of $\boldsymbol{E}_{s2}$ and $\boldsymbol{E}_{s4}$ is shown in Fig. 5b1 and b3. The above situation shows that multiple peaks caused by dressing effect are direct evidence of frequency multimode [28]. From single-dressing effect to double-dressing effect, the increase of dressing effect will increase the frequency mode.

Next, we study the multicomponent signal and background obtained by scanning the detuning Δ_{s1} of the probe field $\boldsymbol{E}_2$ when the detuning Δ_1 of $\boldsymbol{E}_1$ is discretely changed in Fig. 6. In Fig. 6a–c, the detuning Δ_1 varies from − 1.95 to − 0.95 GHz with step of of 0.1 GHz. The signal in Fig. 6a is the superposition result of the fluorescence signal and gain peaks ($|\rho_{FL}{}^{(2)}|^2 + |\rho_{S3}{}^{(3)}|^2$). The curve of fluorescence signal is presented as a dip, which is formed by the dressing effect of $\boldsymbol{E}_2$ ($G_2^2/[\Gamma_{22} + i(\Delta_{s2} - \Delta_2)]$). As the absolute value of detuning Δ_1 becomes smaller, the dip deepens and has a maximum value at − 1.75 GHz, then shallows. And the profile of fluorescence signal in Fig. 6a shows a peak (Eq. 11) with a range of 500 MHz, and a center frequency of − 1.75 GHz. The intensity of the gain peak ($|\rho_{S3}{}^{(3)}|^2$) increases with decrease in the absolute value of Δ_1 (Eq. (4)). Figure 6a1 and a2 shows the cases where the fluorescence and gain peak signals coexist ($|\rho_{FL}{}^{(2)}|^2 + |\rho_{S3}{}^{(3)}|^2$). To make the description clearer, we simulated the fluorescence signal ($|\rho_{FL}{}^{(2)}|^2$), the gain peak signal ($|\rho_{S3}{}^{(3)}|^2$), and the total superimposed signal ($|\rho_{FL}{}^{(2)}|^2 + |\rho_{S3}{}^{(3)}|^2$), as shown in Fig. 6e1 and e2. The experimental results are consistent with the theory.

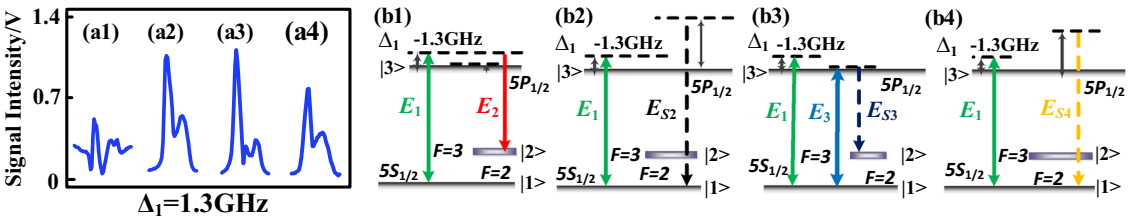

Fig. 5 Measured signal intensity versus laser $\boldsymbol{E}_2$ frequency detuning Δ_{s1} when pumping frequency detuning Δ_1 is set at − 1.3 GHz

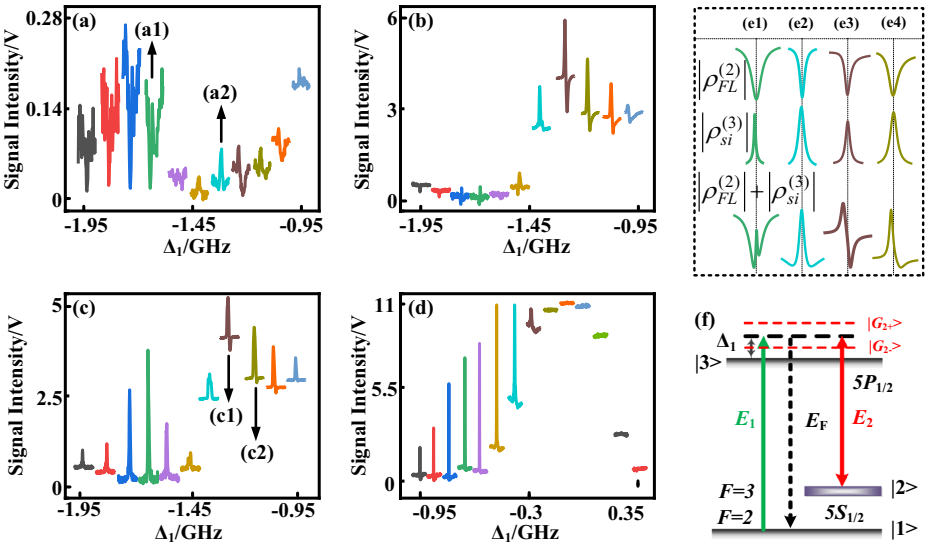

Fig. 6 Measured signal intensity curves of the detuning Δ_{s1} of the probe field $\boldsymbol{E}_2$ at different pump fields $\boldsymbol{E}_1$ detuning Δ_1. **a** The "a" signal in the cascade I channel. **b** The "a" signal in the cascade II channel. **c** The "b" signal in the cascade II channel. From left to right, these three figures are changing Δ_1 from − 1.95 to − 0.95 GHz. **d** The "a" signal in the probe channel. From left to right, changing the detuning Δ_1, from -0.95 GHz to -0.35 GHz. **e1** and **e2** represent theoretical simulations of Figures **a1** and **a2**. **e3** and **e4** represent theoretical simulations of the graphs **c1** and **c2**. **f** Single-dressing fluorescence energy level

Figure 6b and c shows the a and b signals in the $\boldsymbol{E}_{s4}$ channel under the same experimental conditions. The $\boldsymbol{E}_{s4}$ signals include the superposition of fluorescence signal and gain peaks ($|\rho_{FL}^{(2)}|^2+|\rho_{S4}^{(3)}|^2$). Specifically, the theoretical superposition simulation diagram of Fig. 6c1 and c2 is shown in Fig. 6e3 and e4, which shows that the experimental results are consistent with the theoretical simulation. Comparing Fig. 6b and c shows that the fluorescence dip in Fig. 6b is deeper at the same Δ_1, which indicates that the "a" signal in Fig. 6b is subjected to a stronger dressing effect than the b signal.

In Fig. 6d, the $\boldsymbol{E}_{S1}$ signal by scanning Δ_{s1} at different values of Δ_1 in a large range varies from − 0.95 to 0.35 GHz from left to right in 0.1 GHz intervals. The background of signals in Fig. 6d shows a Doppler fluorescence peak with a background range of 700 MHz and a center frequency of 0.175 GHz. When the detuning Δ_1 gradually approaches the resonance, the intensity of gain peak first increases and then decreases. This due to the Eq. (7), as the detuning Δ_1 decreases, the intensity of the gain peak increases. But when the Δ_1 is too close to the resonance, the gain peak is absorbed resulting to a decrease in intensity.

Finally, we investigate the line shift of the PA-CFWM signal resonant frequency through different parameters (Δ_1, power $\boldsymbol{E}_1$ (P_1) and angle α between $\boldsymbol{E}_1$ and $\boldsymbol{E}_3$). In Fig. 7a, from bottom to top, the value of Δ_1 is − 1.45 GHz, − 1.35 GHz, − 1.3 GHz, − 1.2 GHz, and − 1.05 GHz, respectively. The dip of each sub-curve represents the EIA (bright state), which satisfies the enhancement condition $\Delta_2-(\Delta_1+(\Delta_1^2+4|G_1|^2)^{1/2})/2=0$.The peak is third-order gain peak, which is related to Eq. (7). As the detuning Δ_1 decreases, the intensity of EIA signal in Fig. 7a can be described with the term $iG_2/\left[(\Gamma_{32}+i\Delta_{s1})+|G_1|^2/[\Gamma_{12}+i(\Delta_{s1}-\Delta_1)]\right]$, the EIA dip gradually shallows, the intensity of the gain peak increases. When the Δ_1 = -1.3 GHz, the signal is composed of EIA dip and third-order gain peaks ($I_0-|\rho_{s1}^{(1)}|^2+|\rho_{S1}^{(3)}|^2$). However, when the Δ_1 = -1.05 GHz, only the third-order gain peak can be observed. The position of the resonant peak shifts in the direction of $d\Delta_{s1}/d\Delta_1=3/4+(\varepsilon+G_1)/4((\varepsilon+G_1)2+4{G_1}^2)^{1/2}$, where $\varepsilon=\Delta E/\hbar$, G_1 represents the intensities of the dressing fields $\boldsymbol{E}_1$, which affects not only the signal intensity but also the resonance position; and the line shift of the signal can be directly described by the equation. By analyzing the equation, we can conclude that the line shift satisfies $3/4<|d\Delta_{s1}/d\Delta 1|<2$. These results manifest a negative correlation between Δ_2 and Δ_1 with a large shift in the linear speed.

Figure 7b–c shows the measured $\boldsymbol{E}_{s1}$ signals and $\boldsymbol{E}_{s4}$ signals by scanning Δ_2 at different discrete values of P_1. From bottom to top, the value of P_1 is 50 mW, 70 mW, 110 mW, 130 mW, and 147 mW, respectively. Similar to EIA in Fig. 7a, the EIA dip of Fig. 7b becomes shallow due to increasing G_1 in the denominator term. And the intensity of gain peak in Fig. 7b increases and gradually oscillates to form multiple peaks. According to Eq. (10), the gain peak in Fig. 7c can increase with G_1. Specially, the increase of P_1 increases the nonlinear effect of the system to show a periodic oscillation peak with dynamic instability [33]. In addition, the position of the resonant peak shifts in the direction of $dG_1/d\Delta_{s1}=1/(3/2+(\varepsilon+G_1)/((\varepsilon+G_1)^2+4{G_1}^2)^{1/2}$, the shift rate of power $\boldsymbol{E}_1$ to Δ_2 satisfying $0<|dG_1/d\Delta_{s1}|<1$.

As with Fig. 7d–e, $\boldsymbol{E}_{s1}$ signal and $\boldsymbol{E}_{s4}$ signal can be measured by scanning Δ_2 at different discrete values of angle α between $\boldsymbol{E}_1$ and $\boldsymbol{E}_3$. Altering the angle α is equivalent to introducing a phase factor $e^{i\Phi}$ into the dressing term, the corresponding dressing item can be expressed as ${G_1}^2e^{i\Phi}/(\Gamma_{32}+i\delta_2+i\Delta_1)$. The EIA signal and the third-order gain peak are present in Fig. 7 (d), and the third-order gain signal is shown in Fig. 7e. From bottom to top, due to the change of angle α, the dressing effect first decreases, then increases and then decreases, and the intensity of the gain peak first increases, then decreases and then increases (Fig. 7d). In Fig. 7e, the double peaks are caused by G_1 dressing effect, and the conversion of left and right peaks indicates the conversion of light and dark states. The line shift rate of α can be expressed as $d\alpha/d\Delta_2=1/((3/2G_1+1/({G_1}^2))^{1/2})\cos\Delta\Phi$, which satisfying $0<|d\alpha/d\Delta_{s1}|<1$. By comparing the line shift of Δ_2 with Δ_1, power $\boldsymbol{E}_1$ and angle α between $\boldsymbol{E}_1$ and

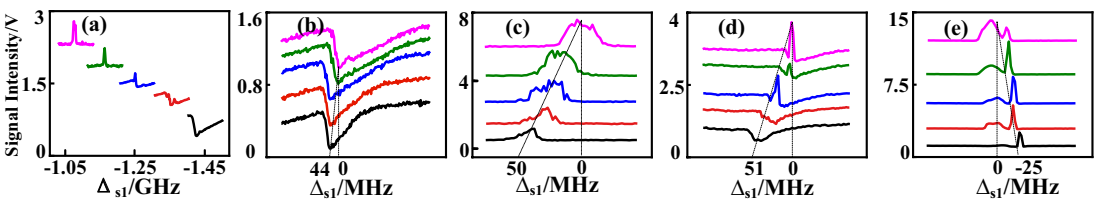

Fig. 7 Similar to Fig. 6. **a** The b signal in the probe channel. From bottom to top, change the detuning Δ_1 from − 1.45 to − 1.05 GHz. **b**, **c** The b signal in the probe channel and cascade I channel. From bottom to top, change the power of $\boldsymbol{E}_1$ from 50 to 147 mW. **d**, **e** The b signal in the probe channel and cascade I channel. From bottom to top, changing the angle between $\boldsymbol{E}_1$ and $\boldsymbol{E}_3$, moving vertically

E_3, it can be known that the line shift of changing Δ_1 is much larger than that of changing the power E_3 and angle α. This is because the position of the Δ_1 will directly affect the position of the Δ_{s1}, while the power E_1 and angle α only affect the dressing field, the effect on the line shift will be smaller. But the adjustment of all three parameters can cause light–dark state conversion. The above research results can be applied to optical communication. Moreover, multipeaks appear when adjusting the parameters (Δ_1, power E_1 (P_1) and angle α between E_1 and E_3), indicating that regulation of these three parameters in dressing items can appear frequency multimode.

3.2 Spatial multimode analysis

In this section, we will explore the properties of spatial multimode. With probe field E_2 injected to this system, E_{s1}, E_{s2}, E_{s3}, E_{s4} signals are amplified. The spatial images by changing power E_3 and detuning Δ_1 are shown in Fig. 8a, b, respectively. And Fig. 8c, d shows the spectrum of E_{s1}, E_{s2}, E_{s3}, E_{s4} signals corresponding to Fig. 8a, b, respectively. As shown in Fig. 8a1, a2, the spot areas at E_{s1}, E_{s2}, E_{s3}, E_{s4} signal channels were all approximately doubled with increasing power E_3. This is because the detuning $\Delta_1 = -1.7$ GHz of the spatial spots (Fig. 8a1, a2) is in the defocusing region ($\Delta n < 0$)[29]. As the power E_3 increases, the Kerr effect of the spatial spot increases (Eq. 19), so the area of the spot increases due to defocusing effect. Since the number of spatial modes can be obtained from the phase-matching area and the area ratio of a single mode [27], the number of spatial modes in all single channels is also doubled, and can be estimated to be more than 800.

When the detuning Δ_1 approaches resonance, the spatial spots at E_{s1}, E_{s2}, E_{s3}, E_{s4} signal channels not only increased the area but also split unevenly to more spots (Fig. 8b1, b2). This is because, as the detuning Δ_1 changes from $\Delta_1 = -1.7$ GHz to $\Delta_1 = -1.2$ GHz ($\Delta n < 0$), the Kerr effect increases as shown in Eq. (20), thus increasing the defocusing effect of spatial spot. Therefore, the spatial spot area increases or even split. Similarly, all single channels can, on total, reach more than 1200 spatial modes.

As shown in Fig. 8c, the signals of E_{s1}, E_{s2}, E_{s3}, and E_{s4} all split into two peaks from the red signal curve ($P_3 = 35$mw) to the signal blue curve ($P_3 = 50$mw). This can be explained by the enhanced dressing effect of E_3, which splits the energy level $|1>$ into $|G_{3+}>$ and $|G_{3-}>$; thus, the E_{s1}, E_{s2}, E_{s3}, E_{s4} signals are split into double peaks. The double peaks in red signal curve of Fig. 8d should be caused by the E_3 single-dressing effect. When the detuning Δ_1 is close to the resonance, the E_{s1}, E_{s2}, E_{s3}, E_{s4} signals are split into three peaks. This is due to the detuning Δ_1 approaching resonance, the dressing effect of E_1 increases, splitting the energy level $|G_{3-}>$ into $|G_{1-+}>$ and $|G_{1-}>$, the corresponding dressing energy-level diagram of ^{85}Rb as shown in Fig. 8g, so the three peaks can be observed. The existence of multiple peaks represents the existence of frequency multimode, and the increase in the number of peaks indicates the increase in the number of frequencies modes. Whether changing P_3 or detuning Δ_1, the dressing effect is increased; thus, the dressing effect increases the frequency modes.

Figure 8e–f shows the evolution of spontaneous spatial spot with different detuning Δ_1 in the single and double pump field, respectively. As the detuning Δ_1 approaches the resonance, the spatial spot gradually defocuses due to the Kerr effect, and the spatial spot splits into multiple parts. In Fig. 8e3, the spot shows a spontaneous four-wave mixing process, and the spot shows a two-cascade spontaneous four-wave mixing process in Fig. 8f3. Compared with Fig. 8e3, the number of spatial spot splitting in Fig. 8f3 is much higher, which indicates that the dressing field can get more spatial modes.

The relationship between frequency domain and spatial domain can be reflected by the expression $\delta \boldsymbol{k}_i = \delta_i n/c$. It shows that the frequency coherent channel and the spatial coherent channel correspond to each other. As shown

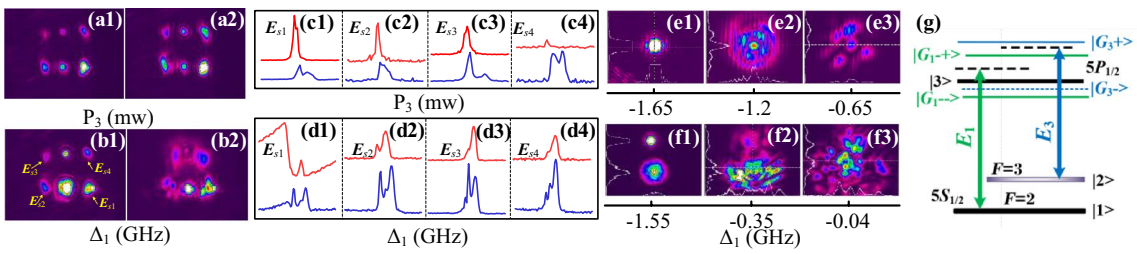

Fig. 8 **a1**, **a2** Injected spatial images by changing $P_3 = 35$mw to $P_3 = 50$mw, respectively. **b1**, **b2** Injected spatial images by changing $\Delta_1 = -1.7$ GHz to $\Delta_1 = -1.2$ GHz, respectively. **c1**–**c4** Measured signal intensity of E_{s1}, E_{s2}, E_{s3} and E_{s4} versus Δ_2, from top to bottom, by changing $P_3 = 35$mw to $P_3 = 50$mw, respectively. **d1**–**d4** Measured signal intensity of E_{s1}, E_{s2}, E_{s3}, and E_{s4} versus Δ_2, from top to bottom, by changing $\Delta_1 = -1.7$ GHz to $\Delta_1 = -1.2$ GHz, respectively. **e1**–**e3** Spontaneous spatial images of single pump field by changing different Δ_1. **f1**–**f3** Spontaneous spatial images of double pump field by changing different Δ_1. Experimental parameters: $P_1 = 133$ mW, $P_2 = 197$ μW, $P_3 = 45$ mW, and $T_{Rb} = 125$ °C. **g** Double dressing energy level

in Fig. 3, the number of peaks and the rings increase and correspond one to one as the dressing effect increases. The relationship of δ_i and $\delta \boldsymbol{k}_i$ demonstrates the concord of multimode in both frequency and spatial domains. Because the probe field is a single longitudinal mode, every amplified signal channel in Figs. 8(a)–(b) is equivalent to a peak in Fig. 8c, d, respectively. Therefore, the splitting of the spatial spot in Fig. 8a, b can only be due to the Kerr effect. Moreover, the number of coherent channels obtained from the sum of each set of signal peaks in Fig. 8c, d should be on the same order of magnitude as the number of spots generated by the spontaneous cascade four-wave signals in Fig. 8f. But when considering the Kerr effect, the number of spontaneous spatial spot divisions will be more. Therefore, the frequency domain and the spatial domain have a good correspondence on the dressing coherent channel, and when the dressing effect is larger, the frequency multimode and the spatial multimode both will increase.

4 Conclusion

In summary, this study investigates the properties of four quantum correlated beams generated through the PA-CFWM process in rubidium vapor. The research explores the signal excitation efficiency of different energy levels by scanning the probe detuning and identifies three different ways to light up the cascade four-mode process. The energy-level with high gain can be selected to produce multimode quantum states, and two pairs of EPR entangled light fields are generated, resulting in quantum correlation between two previously uncorrelated signals. The multimode characteristics of output signals are observed in the frequency and spatial domain. The multimode characteristic is reflected as the multipeak of the spectral signal, and in the spatial domain, the multimode properties appear as an increase of the spatial spot area and a splitting of the spatial spot. The number of frequency multimode and spatial multimode can be controlled through the dressing effect, with the number of spatial modes in four entangled beams reaching up to 1200. Furthermore, the line shift of the PA-CFWM signal resonant frequency can be controlled through experimental parameters such as the detuning and power of the dressing field. These results are important not only for fundamental tests of quantum effects but also for their numerous possible applications in quantum technologies, such as quantum imaging and quantum metrology, opening up possibilities for future research in quantum communication and quantum information processing.

Acknowledgements This work was supported by the National Key Research and Development Program of China (2017YFA0303700, 2018YFA0307500), Key Scientific and Technological Innovation Team of Shaanxi Province (2021TD-56), National Natural Science Foundation of China (61975159, 12174302, 62022066, 12074306, 12074303).

Author contributions Jiajia Wei and Yufeng Li: wrote the main manuscript text and prepared figures 1-8. Binshuo Luo: Validation, Formal analysis. Jiaxuan Wei: Validation, Formal analysis. Haitian Tang: Validation, Formal analysis. Zhou Feng: Funding acquisition, Data curation. Changbiao Li: Conceptualization, Methodology. Yanpeng Zhang: Conceptualization, Methodology. All authors reviewed the manuscript.

Data availability The data that support the findings of this study are available from the corresponding author upon reasonable request.

Declarations

Conflict of interest The authors declare no conflicts of interest.

References

1. C. Monroe, Nature **416**, 238 (2002)
2. N. Treps, U. Andersen, B. Buchler, P.K. Lam, A. Maitre, H.-A. Bachor, C. Fabre, Phys. Rev. Lett. **88**, 203601 (2002)
3. M. Bourennane, M. Eibl, S. Gaertner, C. Kurtsiefer, A. Cabello, H. Weinfurter, Phys. Rev. Lett. **92**, 107901 (2004)
4. H. Hübel, D.R. Hamel, A. Fedrizzi, S. Ramelow, K.J. Resch, T. Jennewein, Nature **466**, 601–603 (2010)
5. G. Brida, M. Genovese, A. Meda, I.R. Berchera, Phys. Rev. A **83**, 033811 (2011)
6. P.G. Kwiat, K. Mattle, H. Weinfurter, A. Zeilinger, A.V. Sergienko, Y. Shih, Phys. Rev. Lett. **75**, 4337 (1995)
7. X. Jia, Z. Yan, Z. Duan, X. Su, H. Wang, C. Xie, K. Peng, Phys. Rev. Lett. **109**, 253604 (2012)
8. Y.P. Zhang, Z.Q. Nie, H.B. Zheng, C.B. Li, J.P. Song, M. Xiao, Phys. Rev. A **80**, 013835 (2009)
9. J.K. Thompson, J. Simom, H. Loh, V. Vuletić, Science **313**, 74 (2006)
10. R.C. Pooser, A.M. Marino, V. Boyer, K.M. Jones, P.D. Lett, Phys. Rev. Lett. **103**, 010501 (2009)
11. S. Du, J. Wen, M.H. Rubin, G.Y. Yin, Four-wave mixing and biphoton generation in a two-level system. Phys. Rev. Lett. **98**, 5053601 (2007)
12. D.R. Hamel, L.K. Shalm, H. Hübel, A.J. Miller, F. Marsili, V.B. Verma, R.P. Mirin, S.W. Nam, K.J. Resch, T. Jennewein, Nat. Photonics **8**, 801 (2014)
13. D. Ding, W. Zhang, S. Shi, Z. Zhou, L.I. Yan, B. Shi, G. Guo, Optica **2**, 642 (2015)
14. J. Wen, E. Oh, S. Du, J. Opt. Soc. Am. B **27**, 000A11 (2010)
15. Z.Q. Nie, H.B. Zheng, P.Z. Li, Y.M. Yang, Y.P. Zhang, M. Xiao, Phys. Rev. A **77**, 063829 (2008)
16. Z.Y. Zhang, F. Wen, J.L. Che, D. Zhang, C.B. Li, Y.P. Zhang, M. Xiao, Sci. Rep. **5**, 15058 (2015)
17. V. Boyer, A.M. Marino, R.C. Pooser, P.D. Lett, Chem. Phys. Chem. **10**, 755–760 (2009)
18. N. Corzo, A.M. Marino, K.M. Jones, P.D. Lett, Opt. Express. **19**, 21358–21369 (2011)
19. Z. Qin, J. Jing, J. Zhou, C.J. Liu, R. Pooser, Z.F. Zhou, W.P. Zhang, Opt. Lett. **37**, 3141–3143 (2012)
20. V. Boyer, A.M. Marino, R.C. Pooser, P.D. Lett, Science **321**, 544 (2008)
21. Z. Qin, L. Cao, H. Wang, A.M. Marino, W. Zhang, J. Jing, Phys. Rev. Lett. **113**, 023602 (2014)
22. E.M. Knutson, J.D. Swaim, S. Wyllie, R.T. Glasser, Phys. Rev. A **98**, 013828 (2018)

23. H. Wang, C. Fabre, J. Jing, Phys. Rev. A **95**, 051802 (2017)
24. S. Liu, H. Wang, J. Jing, Phys. Rev. A **97**, 043846 (2018)
25. F. Devaux, E. Lantz, Eur. Phys. J. D. **8**, 117–124 (2000)
26. N.V. Corzo, A.M. Marino, K.M. Jones, P.D. Lett, Phys. Rev. Lett. **109**, 043602 (2012)
27. D.Y. Zhu, Y.H. Yang, D. Zhang, R.Z. Liu, D.M. Ma, C.B. Li, Y.P. Zhang, Sci. Rep. **7**, 43689 (2017)
28. X.H. Li, J. Wu, S. Xiong, M. Chen, H. Yan, Z.G. Wang, Y.P. Zhang, Photon. Res. **7**, 1454–1460 (2019)
29. Y.P. Zhang, C.C. Zuo, H.B. Zheng, C.B. Li, Z.Q. Nie, J.P. Song, H. Chang, M. Xiao, Phys. Rev. A **80**, 055804 (2009)
30. E.A. Rojas-González, A. Borne, B. Boulanger, J.A. Levenson, K. Bencheikh, Phys. Rev. Lett. **120**, 043601 (2018)
31. Y. Zhang, H. Wang, X.Y. Li, J.T. Jing, C.D. Xie, K.C. Peng, Phys. Rev. A **62**, 023813 (2000)
32. C.B. Li, Y.F. Li, W. Li, K.K. Li, Y.L. Liu, Y. Cai, Y.P. Zhang, New J. Phys. **24**, 093022 (2022)
33. H. Hübel, D.R. Hamel, A. Fedrizzi, S. Ramelow, K.J. Resch, T. Jennewein, Nature **466**, 7306 (2010)
34. Y. Feng, K.K. Li, A. Irfan, Y.M. Li, W. Li, G.C. Lan, Y.P. Zhang, Annalen. Phys. **531**, 1900072 (2019)